

See discussions, stats, and author profiles for this publication at: <https://www.researchgate.net/publication/263983798>

Oxidation of Magnesia-Supported Pd₃₀ Nanoclusters and Catalyzed CO Combustion: Size-Selected Experiments and First-Principles Theory

ARTICLE in THE JOURNAL OF PHYSICAL CHEMISTRY C · APRIL 2012

Impact Factor: 4.77 · DOI: 10.1021/jp301314s

CITATIONS

22

READS

10

8 AUTHORS, INCLUDING:



Bokwon Yoon

Georgia Institute of Technology

39 PUBLICATIONS 2,883 CITATIONS

SEE PROFILE



Uzi Landman

Georgia Institute of Technology

493 PUBLICATIONS 24,123 CITATIONS

SEE PROFILE



Ueli Heiz

Technische Universität München

91 PUBLICATIONS 4,541 CITATIONS

SEE PROFILE



Michael Walter

Fraunhofer-Gesellschaft zur Förderung der an...

64 PUBLICATIONS 2,488 CITATIONS

SEE PROFILE

Oxidation of Magnesia-Supported Pd₃₀ Nanoclusters and Catalyzed CO Combustion: Size-Selected Experiments and First-Principles Theory

Bokwon Yoon and Uzi Landman*

School of Physics, Georgia Institute of Technology, Atlanta, Georgia 30332-0430, United States

Vahideh Habibpour, Chris Harding, Sebastian Kunz, and Ueli Heiz

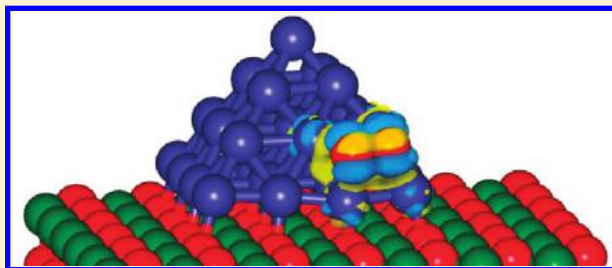
Technische Universität München, Lehrstuhl für Physikalische Chemie – Catalysis Research Center, Lichtenbergstraße 4, 85748 Garching, Germany

Michael Moseler^{†,‡} and Michael Walter[‡]

[†]Freiburg Materials Research Center, University of Freiburg, Stefan-Meier-Str. 21, 79104 Freiburg, Germany

[‡]Fraunhofer Institute for Mechanics of Materials IWM, Wöhlerstr. 11, 79108 Freiburg, Germany

ABSTRACT: Experimental and theoretical investigations of the oxidation reaction of CO to form carbon dioxide, catalyzed by size-selected Pd₃₀ clusters soft-landed on MgO(100), are described. The consequences of pretreatment of the deposited clusters with molecular oxygen, ¹⁶O₂, at a temperature of ~370 K followed by annealing at around 450 K are explored. Subsequent to the above pretreatment stage, the system was cooled to 120 K, and after exposure to ¹⁸O₂ and ¹³C¹⁶O the temperature was ramped and a temperature-programmed reaction (TPR) spectrum recorded. The onset of catalyzed combustion of CO starts at a temperature of 180 K, and the TPR spectrum shows oxidation to occur over a broad temperature range, up to 550 K. Using first-principles density-functional theory, the optimal adsorption geometry of the Pd₃₀ cluster on the MgO(100) surface is found to be a square-base pyramidal structure, with an excess electronic charge of 1.25e, originating from the underlying magnesia support, found to be localized near the interfacial region of the cluster with the supporting surface. Structural and energetic properties of a variety of oxygen adsorption sites on the supported palladium cluster and effects due to multiple adsorbed O₂ molecules were explored. It is found that the barriers for dissociation of the adsorbed molecules depend strongly on the locations of the adsorption sites, with very small (<0.1 eV) dissociation energy barriers found for adsorption sites on the Pd₃₀ cluster that are closer to its interface with the Mg(100) surface. This correlates with our finding that adsorption at these interfacial sites is accompanied by excess charge accumulation on the adsorbed molecule through excess partial (0.25e) occupation of the molecular antibonding 2π* orbital, resulting in activation of the molecule to a peroxo-like state. This activation mechanism depletes the excess charge on the cluster, resulting in a self-limiting partial oxidation of the cluster. The information obtained through isotope labeling in the TPR experiments is explored through first-principles quantum simulations of various reaction pathways, with a focus on the multiple coadsorption system Pd₃₀O₁₀(CO)₁₃/MgO. These theoretical calculations allow us to correlate the measured isotope and temperature-dependent TPR features, with operative Langmuire–Hinshelwood, LH, and Mars–van Krevelen-type (MvK) reaction mechanisms, catalyzed by the partially oxidized cluster. The LH mechanism was found to contribute to the reaction at lower temperatures, while the MvK dominates for higher temperatures.



1. INTRODUCTION

Platinum-group metals, e.g., Pt, Pd, Ir, Ru, and Rh, are known to effectively catalyze a large number of chemical reactions. Most often, these metals are used as oxide-supported small particles for oxidation reactions in the chemical industry, in automotive emission control, and in energy-related technologies.^{1,2} Among these reactions, the oxidation of carbon monoxide has been studied rather intensively (see, e.g.,

citations in refs 3 and 4), starting from the early work of Langmuir in the 1920s.⁵ Interestingly, Langmuir proposed that the reaction proceeded via the so-called Eley–Rideal (ER) mechanism⁶ (where the reaction advances via a collision

Received: February 9, 2012

Revised: April 2, 2012

Published: April 5, 2012



between an impinging gas-phase molecule and an adsorbed species), whereas now the reaction is understood^{3,7} to be controlled by the Langmuir–Hinshelwood (LH) mechanism,⁸ where the reaction occurs through interactions among adsorbed molecules, radicals, or fragments of the reactant molecules.

It is pertinent (particularly in light of our forthcoming discussion of oxidation processes of Pd nanoparticles) to discuss here the early development of an additional idea pertaining to catalytic activation mechanisms, where, unlike the case of the other two mechanisms (ER and LH) mentioned above, a component of the catalyst's lattice appears in the reaction product. The first recorded description of such a mechanism has been published (apparently⁹ as early as in 1922) by Pease and Taylor who summarized their study¹⁰ of copper-catalyzed oxidation of hydrogen as follows: “the results are believed to be satisfactorily explained by assuming that the combination takes place mainly as a result of the alternative oxidation and reduction of the catalyst”. A similar mechanism, where lattice oxygen enters the desorbable reaction products, was formulated more explicitly a decade later.¹¹ The importance of the idea that oxygen is not simply added to the reductant but is transformed prior to that into a lattice oxygen (with the ability to separate the processes of oxygen depletion and subsequent replenishment into two consecutive steps) did not gain a following for quite a while.⁹ This state of affairs changed after the publication of the paper¹² by Mars and van Krevelen (MvK) in 1954 and subsequent successful application of the MvK mechanism in a series of kinetic studies^{13,14} (see review of the MvK mechanism in ref 9).

Palladium is one of the most often employed metals in catalysis,¹⁵ particularly because of its use in three-way catalysts in automotive exhaust systems¹⁶ and the environmental great interest in efficient, low-temperature, Pd-catalyzed oxidative conversion of noxious exhaust gases (e.g., CO, NO_x, and hydrocarbons) emitted by internal combustion engines to less harmful gases.¹⁷ In the following we will focus mainly on oxidation studies (mostly CO combustion) catalyzed by palladium.

With the development, about the mid-20th century, of experimental surface science characterization techniques (structural, electronic, and vibrational spectroscopies), fundamental experimental and theoretical investigations into the microscopic origins of chemical reactivity and catalytic activity focused largely on extended single surfaces, often under ultrahigh vacuum conditions. However, as aforementioned, industrial catalytic processes involve supported metal particles (with sizes ranging, roughly, from subnanometer to dozens of nanometers in diameter) that are oxidized in the course of the reaction. Consequently, a comprehensive understanding of the oxidation mechanisms and oxidation states of the metal cluster catalysts and their influence on the catalytic activity is imperative for the rational design of efficient catalysts and optimization of their operational conditions (see review in ref 18).

The activity, selectivity, and specificity of oxidation catalysts is often found not only to be governed by the size, morphology, and structure of the catalyst but also show a dependence on the chemical nature of the catalyst's surface, which may differ in the presence of oxygen (depending on oxygen pressure and temperature) from its native (bare) state. This is the case even for the relatively simple case of single-crystal surfaces of transition metals (see citations 3–20 in ref 19).

To highlight, we note here that, indeed, the importance of intermediate surface oxide phases has been recognized rather recently.²⁰ This work was followed by investigations of different oxygen species on palladium surfaces,²¹ as well as their interactions with reactants such as CO. In a systematic experimental study,²² it was found that the type of palladium surface oxide may be the determining factor controlling the catalytic reaction pathway and that chemisorbed oxygen serves as a most reactive species with a chemisorbed O(ad) layer enabling the coadsorption of CO(ad). Consequently, the oxidation reaction proceeds via a LH reaction mechanism. This finding is consistent with early Pd(111) single-crystal experiments^{3,23} on the oxidation of CO, where, as aforementioned, it has been proposed: (i) that a LH mechanism between adsorbed oxygen and carbon monoxide dominants and (ii) that adsorbed CO inhibits oxygen adsorption, and consequently CO desorption is the rate-determining step. Interestingly, in the experiments noted above,²² the stoichiometric PdO was found to be essentially nonreactive (compared to the reactivity of the nonstoichiometric oxygenated species), and it has been shown to reduce only at much harsher conditions, requiring 10 mbar of CO and temperatures around 520 K. This has been interpreted as originating from the absence of CO adsorption sites and due to inhibited mass transport to the metal through the oxidic phase, in comparison to the nonstoichiometric Pd₅O₄ surface oxide.

The situation becomes even more involved in the case of surface-supported transition metal catalyst particles. Indeed, for these systems the nature of the oxidic species formed upon exposure to oxygen is likely to be influenced by the interaction of the metal particle with the underlying support^{24–26} (commonly metal-oxide) and by finite size effects. These may be described as having their origins in: (i) structural considerations, e.g., modified atomic arrangements,²⁶ the presence of various facets, edges, and corners, defects, and structural fluxionality²⁷ (that is, variation of the metal particle structure in the course of reaction), and/or (ii) electronic factors, that is, changes in energy level spacing and/or charging^{28,29} effects.

Oxidation processes of palladium particles supported on metal-oxide surfaces have been extensively studied for a model catalyst system with size distributions of the supported particles in the several nanometers range.^{19,30,31} Molecular beam experiments with 4–10 nm Pd particles on Fe₃O₄ at *T* = 500 K suggest the formation of the Pd oxide at the particle/support interface and the chemisorption of oxygen on the metallic upper part of the supported nanoparticles.³¹ Both oxygen species contribute to the CO combustion. The same study deduced, for Pd particles with diameters smaller than 3 nm, complete oxidation to PdO at high temperatures. This finding is in line with high-energy X-ray studies of the size-dependent oxidation of Pd nanoparticles on MgO(100)³² at *T* = 500 K. For oxidation temperatures higher than 500 K, large amounts of oxygen can be “stored” in the model catalyst in the form of a thin Pd-oxide layer at the particle–support interface. The stored oxygen can be reversibly accumulated and depleted, providing an “oxygen reservoir” for catalytic surface reactions.³³ Finally, for temperatures of up to 450 K it has been found that oxygen chemisorbs dissociatively on the metallic Pd surface areas. The oxidation process of the supported Pd particle initiates at the particle support interface, and from there it proceeds to the facet areas of the supported particle that are further distanced from the underlying surface. This has

significant effects on the CO oxidation reaction. At low temperatures (<450 K), CO oxidation occurs mainly on metallic Pd surface areas. However, the activity of Pd surface oxides is drastically lower, and its formation may even deactivate the catalyst.¹⁹ We remark that the CO combustion reaction scheme used in the interpretation of the above molecular beam experiments from 4 to 10 nm supported Pd particles, involving formation of certain surface oxide species on the partially oxidized Pd particle, which is subsequently reduced via direct reaction with adsorbed CO or through decomposition and subsequent migration to a reaction site where the oxygen atom combines with adsorbed CO to form CO₂, is akin to an MvK-type mechanism (see discussion at the start of this section).

For a little over a decade, one of the most challenging research directions in catalysis has been the study of reactions catalyzed by nanometer-size clusters (in particular, experiments and theories on size-selected clusters), in the regime where scaling of the probed properties with cluster size does not apply.²⁴ This nonscaling regime pertains to clusters of up to a few dozens of atoms, where the cluster properties (structural, electronic, dynamical, and chemical) vary in a nonmonotonic manner with the number of atoms. Most previous investigations of catalytic activity in this size regime focused on supported and gas-phase gold clusters; see reviews on catalytic reactivity of size-selected supported gold clusters in refs 24 and 25 and refs 34–37 for work on catalysis by size-selected gas-phase gold clusters.

Pertaining to the topic of this paper, we note pulsed molecular beam experiments³⁸ on CO oxidation by size-selected Pd_{*n*}/MgO clusters (*n* < 30), where O₂ dissociation barriers of increasing values have been found for Pd clusters with decreasing sizes, resulting in increasing dissociation rates with increasing temperature. An experimental investigation of temperature-programmed reaction (TPR) of CO with O₂ catalyzed by size-selected Pd clusters (with up to 25 atoms) soft-landed on rutile (TiO₂(110)) revealed³⁹ an interesting correlation between the nonmonotonically varying Pd 3d binding energy (measured with X-ray photoelectron spectroscopy, XPS) and the strongly size varying CO oxidation activity; in these studies measured low activity was correlated with higher-than-expected Pd 3d binding energy. In another study,⁴ the dissociative binding efficiency of O₂ over Pd_{*n*}/TiO₂(110) (*n* = 4, 7, 10, 20) was measured with TPR, mass spectrometry, and XPS, showing that the smaller clusters appear to be generally less efficient at oxygen activation. Variable-temperature measurements showed that the formation of the reactive (adsorbed) oxygen is an activated process for all cluster sizes, with the activation energy varying nonmonotonically with cluster size.

While for the case of supported gold clusters and their activity in catalyzing the oxidation of CO a wealth of theoretical information has been obtained over a period of a decade (see reviews in refs 24 and 25), the properties of supported Pd clusters and their chemical and catalytic characteristics remain, essentially, an uncharted territory. Indeed, the only published theoretical studies to date pertain to: (i) the soft landing of a Pd_{*n*} (*n* = 2–7, 13) cluster on a MgO(100) surface,⁴⁰ (ii) a joint theoretical and experimental (TPR and infrared spectroscopy) investigation of the catalyzed CO oxidation by a single Pd atom anchored at an oxygen vacancy on a MgO(100) surface,⁴¹ and (iii) an investigation of the facile transformations of small magnesia supported Pd clusters to Pd_{*x*}O_{*y*} nanooxides.^{42,43}

In this paper, we report on experimental and theoretical investigations of the oxidation reaction of CO to form carbon dioxide, catalyzed by size-selected Pd₃₀ clusters soft-landed on MgO(100). Experimentally, we investigate the consequences of pretreatment of the deposited clusters with molecular oxygen at a temperature of ~370 K in an ¹⁶O₂ background (*P*_{oxygen} = 5 × 10^{−7} mbar), followed by annealing at around 450 K. Subsequent to the above pretreatment stage, the system was cooled to 120 K. After exposure to ¹⁸O₂ and C¹⁶O, the temperature was ramped, and a temperature-programmed reaction (TPR) spectrum was recorded. In similar experiments for a smaller cluster (Pd₁₃), we have observed that the pretreatment of the supported cluster with oxygen lowered the onset of the CO oxidation reaction compared to the one measured for an untreated cluster. Similarly, we found here for the larger (Pd₃₀) cluster that the catalyzed combustion of CO starts already at a temperature of 180 K and that the TPR spectrum extends over a wide temperature range of up to 550 K.

Using first-principles density-functional theory calculations, we investigated first the adsorption geometry of the Pd₃₀ cluster on the MgO(100) surface. A square-base pyramidal structure was found to be energy optimal, with an excess electronic charge of 1.25e (originating from the underlying magnesia support) found to be localized near the interfacial region of the cluster with the supporting surface. Subsequently, we explored rather exhaustively structural and energetic properties of a variety of oxygen adsorption sites on the supported palladium cluster and effects due to multiple adsorbed O₂ molecules. We show that the barriers for dissociation of the adsorbed molecules depend strongly on the location of the adsorption site on the supported pyramidal Pd₃₀ cluster. The transition state for dissociation is very small (<0.1 eV) for adsorption sites (on the cluster) that are closer to the cluster interface with the Mg(100) surface, and they increase as a function of distance from that interface. Interestingly, we find that for the interfacially adsorbed oxygen molecules adsorption on the supported Pd₃₀ cluster is accompanied by accumulation of excess electronic charge (0.25e per O₂ molecule) on the molecule, manifested by partial occupation of the 2π* antibonding orbital, leading to activation of the O–O bond and its subsequent ready dissociation. We note here that the electronic activation of the first four or five adsorbed oxygen molecules depletes the aforementioned excess interfacial charge, with further adsorbed oxygen molecules activated to a much lesser degree. As a result, the molecules near the cluster/support interface dissociate readily, while further oxygen dissociation processes (occurring at larger distances from the cluster-to-surface interface) entail much larger dissociation barriers, resulting in self-limiting partial oxidation of the Pd₃₀ cluster. Consequently, our theoretical analysis of the CO oxidation reaction focuses on a partially oxidized Pd₃₀O₁₀ cluster.

Using the information obtained through isotope labeling in the TPR experiments (where the two isotopomers, ¹³C¹⁶O¹⁶O and ¹³C¹⁶O¹⁸O, were detected mass spectrometrically during the temperature ramp), we explored through first-principles quantum simulations various reaction pathways, with a focus on the multiply coadsorbed system Pd₃₀O₁₀(CO)₁₃/MgO. These theoretical calculations allowed us to correlate the measured isotope and temperature-dependent TPR features, with operative LH and MvK-type reaction mechanisms catalyzed by the partially oxidized cluster. The LH mechanism was found

to contribute to the reaction at lower temperatures, while the MvK dominates for higher temperatures.

The paper is organized as follows. The experimental and theoretical methods employed in our investigations are described in subsections 2.1 and 2.2, respectively. The results of our study are given in section 3, with those obtained in the experiments (TPR and Fourier transform infrared, FTIR) presented in subsection 3.1 and the theoretical results described in subsection 3.2. Theoretical results pertaining to the bare Pd₃₀ cluster adsorbed on MgO(100) are given in subsection 3.2.1. The adsorption of O₂ on Pd₃₀/MgO and a detailed analysis of the cluster oxidation states are described in subsection 3.2.2. Subsection 3.2.3A is devoted to theoretical results about CO oxidation catalyzed by the aforementioned partially preoxidized Pd₃₀O₁₀(CO)₁₃/MgO cluster, with multiply coadsorbed CO molecules. Subsection 3.2.3B describes the temperature-dependent mechanisms and reaction pathways which we analyze and correlate with the experimental observations. A summary of our results is offered in section 4.

2. METHODS

2.1. Experimental Methods. The model catalysts were prepared by depositing size-selected metal clusters with low kinetic energy (1 eV/atom) onto well-defined MgO films.^{44,45} For each cluster deposition experiment, the magnesium oxide films were prepared in situ by epitaxial growth onto a Mo(100) single crystal.²⁹ The thicknesses of the films were typically around 10 monolayers; ¹⁶O₂ partial pressure, evaporation rate, and growth temperature were 5×10^{-7} mbar, 0.1 ML min⁻¹, and 320 K. Auger electron spectroscopy (AES), metastable helium impact electron spectroscopy (MIES), and ultraviolet photoelectron spectroscopy (UPS) were employed to verify the cleanliness and characterize the electronic states of the oxide layer. The palladium clusters were produced using a high-frequency (120 Hz) laser vaporization source.⁴⁶

The cluster beam was guided by a set of ion optics through differentially pumped vacuum chambers, where the positively charged clusters were deflected by a custom-made, electrostatic ion bender and focused into a quadrupole mass-selecting unit (ABB-Extrel; mass limit 4000 amu). The mass-selected cluster beam is further guided by a set of Einzel lenses and finally soft-landed onto the MgO surface. Neutralization of the clusters upon deposition occurs either at surface defects or via charge tunneling through the thin films.^{29,47} Cluster coverage was less than 0.2% of a monolayer (1 ML $\approx 2.25 \times 10^{15}$ clusters cm⁻²) as measured from the integration of the cluster current during deposition. This ensures the supported clusters to be well isolated; furthermore, substrate temperatures of around 100 K prevent agglomeration.

After deposition and prior to the reactivity studies, the size-selected Pd clusters were oxidized by annealing them at a given temperature (~ 370 K) in an oxygen background of 5×10^{-7} mbar for 1 min. The catalytic performance of the oxidized Pd clusters was then explored using temperature-programmed reaction (TPR) and isotopic labeling experiments. In these experiments, a differentially pumped quadrupole mass spectrometer (Balzers QMG 421) was used to detect the product molecules formed on the model catalyst, while the temperature of the sample was linearly increased at constant rate (~ 2 K/s). To further study the CO combustion on oxidized Pd clusters, infrared measurements of adsorbed carbon monoxide were accomplished by means of a commercial Fourier transform infrared (FTIR) spectrometer (Thermo Nicolet 6700). The IR

radiation was focused onto the sample at grazing incidence with the use of a concave IR-mirror. The reflected IR radiation was detected with a liquid nitrogen-cooled MCT detector (EG&G Optoelectronics). In all measurements, the ¹³CO isotopomer was used as a probe molecule to enhance the signal-to-noise ratio of the measurements, particularly in the TPR experiments. FTIR spectra were recorded over 512 scans with a resolution of 4 cm⁻¹.

2.2. Theoretical Method. To model the Pd₃₀/MgO catalyst system, consisting of a Pd₃₀ cluster supported on a MgO(100) surface and the reactant molecules (oxygen and carbon monoxide), we employed a four-layer MgO(100) slab with a calculational cell consisting of 7×6 unit cells; each layer consisted of 42 Mg and 42 oxygen atoms (see Figure 2), with the atoms in the bottom layer held stationary (at the experimental lattice constant of 4.21 Å) and the atoms in the other three layers allowed to relax to the optimal atomic arrangement; optimal configurations (using a conjugate gradient search) were determined when the calculated forces on the atoms were smaller than 0.001 eV/Å. The bare Pd₃₀ cluster was positioned on the MgO(100) surface, and its configuration was optimized prior to adsorption of the O₂ and CO reactant molecules. The calculational supercell, which included the MgO(100) slab and a 24 Å thick vacuum region, was periodically replicated.

The first-principles electronic structure calculations used the spin-density functional theory (SDFT),^{48,49} with the generalized gradient approximation (GGA)⁵⁰ for the exchange and correlation energy. Ultrasoft pseudopotentials⁵¹ and a plane-wave basis with a cutoff energy of 300 eV were employed, with Γ -point sampling of the Brillouin zone. Since the gas-phase oxygen molecule is paramagnetic and superoxo-like O₂ molecules are involved in the interaction with the palladium cluster and in the CO oxidation reactions, spin polarizations are considered fully in all our calculations; the calculated intramolecular bond lengths of the gas-phase O₂ and CO molecules are 1.237 and 1.145 Å, respectively.

In the first-principles calculations of the reaction profiles (pathways), a reaction coordinate was judiciously chosen; typically, the reaction coordinate consists of the distance between two atoms of the reactant molecules (for example, an O atom of an adsorbed oxygen molecule and the C atom of a reacting CO molecule). For each value of the reaction coordinate, the total energy of the system was optimized through unconstrained relaxation of all of the other degrees of freedom of the system (reactants and other adsorbed molecules, Pd cluster, and MgO substrate atoms). The reaction profiles (reaction paths) were obtained via repeating such calculations for various values of the chosen reaction coordinate. These calculations yield results that are the same as, or close to, those obtained by other methods, e.g., the nudged elastic band and variants thereof; see the discussion on pages 89 and 90 in ref 24.

3. RESULTS

3.1. Experimental Results. Consideration of the possible CO oxidation mechanisms catalyzed by the supported Pd₃₀ clusters led us to focus on two main issues. The first pertains to the extent that oxygen atoms that may have oxidized (at least partially) the palladium clusters during the high-temperature oxygen pretreatment of the supported clusters serve as a source for the combustion of CO (that is, the aforementioned MvK mechanism, see section 1). The second issue concerns the role

of molecular oxygen (i.e., O_2 molecules dosed at cryogenic conditions subsequent to the high-temperature oxygen pretreatment and annealing stage) in the cluster-catalyzed oxidation of CO. As described below, both of these issues can be addressed effectively through isotopic labeling experiments.

The TPR spectra of the $^{13}\text{C}^{16}\text{O}^{16}\text{O}$ and $^{13}\text{C}^{16}\text{O}^{18}\text{O}$ isotopomers obtained for the supported size-selected oxidized Pd_{30} clusters are displayed in Figure 1. In these experiments,

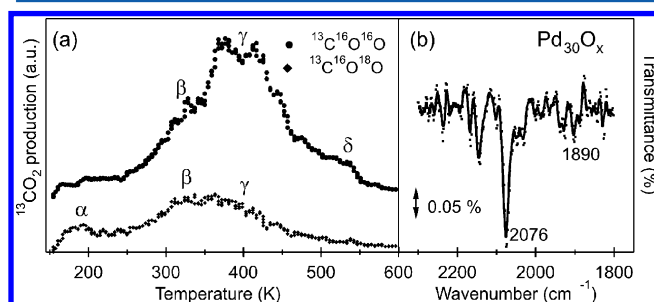


Figure 1. (a) TPR spectra of $^{13}\text{CO}_2$ formation on magnesia-supported palladium oxide clusters (Pd_{30}O_x , $\sim 0.17\%$ ML). The Pd_{30} clusters were oxidized at ~ 370 K in the $^{16}\text{O}_2$ atmosphere, and the temperature ramp was performed after $^{18}\text{O}_2$ and $^{13}\text{C}^{16}\text{O}$ exposure at ~ 120 K. The oxidation products are shown with \bullet ($^{13}\text{C}^{16}\text{O}^{16}\text{O}$) and \blacklozenge ($^{13}\text{C}^{16}\text{O}^{18}\text{O}$) markers. (b) IR spectra of adsorbed $^{13}\text{C}^{16}\text{O}$ on Pd_{30}O_x clusters supported on MgO film. For the measurements presented, a background spectrum (CO free) was subtracted.

the palladium clusters (0.17%) were oxidized at ~ 370 K in a $^{16}\text{O}_2$ background ($P_{\text{oxygen}} = 5 \times 10^{-7}$ mbar) and subsequently annealed at around 450 K. After cooling the sample to 120 K and pumping the residual $^{16}\text{O}_2$ out of the system, the catalyst was exposed to $^{18}\text{O}_2$ and ^{13}CO . During the temperature ramp, the two isotopomers, $^{13}\text{C}^{16}\text{O}^{16}\text{O}$ and $^{13}\text{C}^{16}\text{O}^{18}\text{O}$, were detected mass spectrometrically.

Formation of the $^{13}\text{C}^{16}\text{O}^{16}\text{O}$ isotopomer is associated with a mechanism involving oxygen atoms from the oxidized palladium clusters, and the other isotopomer, $^{13}\text{C}^{16}\text{O}^{18}\text{O}$, is taken to originate from the oxidation of CO by molecular oxygen ($^{18}\text{O}_2$) dosed at cryogenic (120 K) conditions subsequent to the aforementioned high-temperature pretreatment of the cluster. As depicted in the upper spectrum of Figure 1a, the oxidized Pd_{30} clusters contribute to the formation of $^{13}\text{C}^{16}\text{O}^{16}\text{O}$ in a broad temperature window of above 250 K and up to about 550 K. A β mechanism (shoulder) feature is noted at ~ 320 K. Distinct (two) maxima are observed in the desorption spectra around 400 K, and they are labeled as the γ mechanism. Additionally, formation of $^{13}\text{C}^{16}\text{O}^{16}\text{O}$ is observed above 500 K, and it is labeled as the δ -mechanism.

The yield of $^{13}\text{C}^{16}\text{O}^{18}\text{O}$, originating from the reaction of adsorbed CO with cryogenically deposited $^{18}\text{O}_2$, is much smaller than the other isotopomer (see lower spectrum in Figure 1a). The first contribution to the TPR spectrum of this isotopomer is observed below 200 K, and it is labeled as the α -mechanism. The onset of the second (broad) peak appears around 270 K, and it extends up to about 450 K. This contribution may originate from two mechanisms: the lower temperature one, designated by us as the β -mechanism, and the other one (designated as the γ -mechanism) occurring at a higher temperature. These results allow us to conclude that the α -mechanism originates from the presence of cryogenic oxygen (that is, undissociated oxygen molecules, mostly $^{18}\text{O}_2$ deposited under cryogenic conditions), whereas the δ -mechanism is

associated uniquely with the oxidized palladium cluster (that is, it involves oxygen atoms, ^{16}O , originating from the partially oxidized palladium cluster generated during the pretreatment stage). The β - and γ -mechanisms are more complicated, and the isotopic scrambling (evidenced by the observed production of $^{13}\text{C}^{16}\text{O}^{18}\text{O}$ in the temperature range 300–420 K—see β - and γ -peaks in the lower plot in Figure 1(a)) suggests a dynamic exchange of the two different oxygen atoms (coming from oxidized palladium and cryogenically deposited molecular oxygen), occurring on the cluster in the course of the oxidation reaction. Note, however, that the contribution of the palladium atomic oxygen (that is, the oxygen atoms of the oxidized palladium cluster) to the CO oxidation processes is notably higher than that of the molecularly adsorbed oxygen.

To get further insights into the system, the Pd_{30} model catalyst was characterized by FTIR spectroscopy prior to reaction as shown in Figure 1(b). The spectrum was taken at ~ 120 K after oxidation of the deposited Pd_{30} at ~ 370 K in an oxygen background of 5×10^{-7} mbar and saturating the model catalyst with ^{13}CO at cryogenic temperature. The IR spectrum exhibits dominant vibrational frequencies characteristic of ^{13}CO adsorbed in an on-top (2076 cm^{-1}) and possibly a small contribution from a bridge-bonded configuration (1880 cm^{-1}). Interestingly, the oxidized clusters reveal a shift to higher frequencies in comparison to the corresponding metallic palladium clusters; a blue-shift of $\sim 20\text{ cm}^{-1}$ is observed for the on-top bound CO molecule (see Table 1). We also include

Table 1. Vibrational Frequencies of Adsorbed ^{13}CO on Oxidized and Metallic Clusters^a

	experiment		theory		experiment
	O_2 -treated		$\text{Pd}_{30}\text{O}_{10}(\text{CO})_{13}/\text{MgO}$	metallic	metallic
Pd_{30}	2076, 1880	(i)	(top-apex Pd atom)	2012	2055, 1930
		(ii)	(2nd layer from the top)	1895	
		(iii)	(2nd layer from the bottom)	1881	
		(iv)	(edge bridges)	1978	
				1994	

^aFor the metallic clusters, CO adsorption was carried out after cluster deposition, whereas the oxidized clusters were treated at 360 K in an oxygen pressure of 5×10^{-7} mbar prior to CO adsorption. The vibrational frequencies were calculated for CO molecules adsorbed on the partially oxidized palladium cluster $\text{Pd}_{30}\text{O}_{10}\text{CO}_{13}/\text{MgO}$, at the following sites (see Figure 8): (i) on the top-apex Pd atom, (ii) second layer from the top, (iii) second layer from the bottom, and (iv) bottom layer. The calculated vibrational frequencies for CO molecules adsorbed on the metallic system (unoxidized palladium cluster) $\text{Pd}_{30}(\text{CO})_{13}/\text{MgO}$ are: (i) top-apex Pd atom: 2012 cm^{-1} , (ii) 1895 cm^{-1} ; (iii) 1881 cm^{-1} ; (iv) 1978 cm^{-1} . For the partially oxidized cluster ($\text{Pd}_{30}\text{O}_{10}\text{CO}_{13}/\text{MgO}$), the calculated vibrational frequencies were shifted upward by 69 cm^{-1} to account for the difference between the calculated value (2026 cm^{-1}) for the free $^{13}\text{C}^{16}\text{O}$ molecule and the measured⁵² one (2095 cm^{-1}).

in the table theoretical results, obtained through first-principles calculations (see below). The vibrational frequencies calculated for multiple CO molecules adsorbed at various sites on the partially oxidized supported palladium cluster (see Figure 8 below), as well as for the unoxidized (metallic) supported cluster, are in satisfactory agreement with the measured frequencies. In addition, the aforementioned experimentally observed blue shift for the oxidized cluster is reproduced in the

calculations. We also found that the adsorption feature of ^{13}CO typical for on-top bound CO disappears upon CO combustion already at temperatures slightly above 200 K.

3.2. Theoretical Results. As described above, the experimental investigations were carried out on palladium clusters of two sizes, Pd_{13} and Pd_{30} , supported on $\text{MgO}(100)$. In this paper, we focus on theoretical explorations pertaining to the supported Pd_{30} cluster; a complete account of our investigations of the structural and reactive properties of the supported Pd_{13} cluster has been given by us elsewhere (see ref 53).

3.2.1. Bare Pd_{30} Cluster Adsorbed on $\text{MgO}(100)$: $\text{Pd}_{30}/\text{MgO}(100)$. In the clean surface of $\text{MgO}(100)$ (prior to adsorption of the Pd_{30} cluster), the oxygen atoms of the topmost layer are located 0.069 Å higher (i.e., toward the vacuum) than the Mg atoms. After adsorption of the pyramidal Pd_{30} cluster on the surface, the 16 O atoms in the area covered by the base of the cluster (see Figure 2) are found to be located 0.096 Å higher than the corresponding 16 Mg atoms.

The ground-state structure of the supported Pd_{30} cluster is found to be a square pyramid (Figure 2 (a,b)), with the energy of the $\text{Pd}_{30}(\text{pyramid})/\text{MgO}$ system found to be lower by 1.6 eV

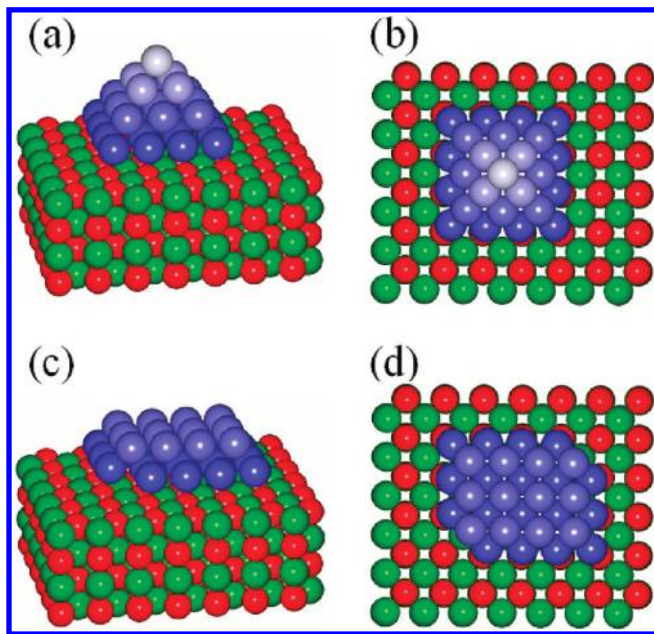


Figure 2. Optimal structures of pyramidal (a,b) and two-layer (c,d) Pd_{30} cluster configurations adsorbed on a $\text{MgO}(100)$ surface. For visual clarity, the atoms of the Pd_{30} clusters are colored by a blue color gradient, depending on the distance of the Pd atoms from the MgO surface, with those closer to the MgO surface depicted in deeper blue color. The Mg atoms are depicted as green spheres and the oxygen atoms as red ones. The adsorbed pyramidal Pd_{30} cluster is 1.6 eV lower in energy than the two-layer cluster. (a) and (b): Pyramidal Pd_{30} . The numbers of Pd atoms from the bottom Pd layer to the top layer are 16, 9, 4, and 1. The spacing between the bottom Pd layer and the topmost O (Mg) atoms under Pd_{30} is 2.275 Å (2.370 Å). The spacing between the bottom (first) layer and the Pd cluster and the layer above it (second layer) is $d_{12} = 1.992$ Å. The spacing between the consecutive layers is $d_{23} = 1.785$ Å and $d_{23} = 1.781$ Å. The average Pd–Pd bond length on the bottom edge of the Pd_{30} pyramid is 2.66 Å. (c) and (d): Two-layer Pd_{30} . The numbers of Pd atoms of lower and upper Pd layers are 18 and 12. The spacing between the lower Pd layer and the topmost O (Mg) atoms under Pd_{30} is 2.257 Å (2.282 Å). The spacing between two Pd layers is $d_{12} = 2.003$ Å.

compared to an alternative two-layer structure (Figure 2(c,d)). On the other hand, the adsorption energy of the Pd_{30} (two-layer) cluster isomer to the $\text{MgO}(100)$ surface is slightly higher ($E_{\text{ads}}(2\text{-layer}) = 8.84$ eV) than that of the pyramidal cluster ($E_{\text{ads}}(2\text{-layer}) = 8.71$ eV); E_{ads} is calculated as the difference between the total energies of the individual components (free cluster and clean surface) and that of the combined adsorption system $\text{Pd}_{30}/\text{MgO}$.

As found in earlier first-principles investigations, free⁵⁴ and supported⁴⁰ Pd clusters exhibit spontaneous magnetization. In the current study, we found that the optimal minimum energy configuration of the Pd_{30} (pyramidal) cluster has a spin state with $N_{\uparrow} - N_{\downarrow} = 4$ (where N_{\uparrow} is the number of up-spin electrons and N_{\downarrow} is the number of down-spin electrons); the energy of this magnetic state is lower by 0.057 eV than that with no magnetic moment, i.e., $N_{\uparrow} = N_{\downarrow}$. On the other hand, after adsorption, the optimal configuration of Pd_{30} (pyramid)/ MgO is characterized by $N_{\uparrow} - N_{\downarrow} = 2$, and it is 0.018 eV lower in energy compared to the nonmagnetic state.

Further insight is obtained from the charge differences between the combined system, calculated first for the bare cluster adsorbed on the MgO surface (see Figure 3(a)) and then for the supported cluster with an O_2 molecule adsorbed in the vicinity of the cluster interface with the MgO surface. From the results in this figure, we conclude that the adsorption of the cluster is accompanied by a transfer of about 1.25 e from the surface to the cluster. The degree of charge transfer from the surface is rather insensitive to the adsorption of an oxygen molecule (compare the values in Figure 3(a) and 3(b)). However, we note that upon oxygen adsorption charge (0.25e) is transferred to the O_2 molecule from the neighboring Pd atoms of the cluster. This excess charge corresponds to increased occupancy of the antibonding $2\pi^*$ orbital of the adsorbed molecule, with consequent activation to a peroxo state characterized by an increased interoxygen bond length ($d(\text{O} - \text{O}) = 1.54$ Å, see Figure 4(a)). Moreover, the adsorption of five oxygen molecules exhausts the excess charge ($\sim 1.25\text{e}$) on the Pd cluster, and consequently, further adsorbed oxygen molecules are activated to a smaller degree, resulting in higher dissociation energy barriers. This contributes to the self-limiting nature of the oxidation process of the supported Pd_{30} nanocluster.

3.2.2. Adsorption of Oxygen on $\text{Pd}_{30}(\text{pyramid})/\text{MgO}(100)$. To explore the interaction of oxygen molecules with the adsorbed $\text{Pd}_{30}(\text{pyramid})/\text{MgO}$ cluster and the oxidation of the cluster, we examined first the properties of various adsorption sites on the surface of the supported cluster; since we focus only on the optimal (pyramidal) configuration of the adsorbed cluster, we omit from here on the “(pyramidal)” label. From a rather exhaustive study, we conclude that essentially all sites on the surface of the bare adsorbed Pd_{30} cluster surface can serve as locations for the adsorption of an O_2 molecule. The most activated adsorption occurs in the second layer bridge configuration (Figure 4(a)) with a binding energy $\text{BE}(\text{O}_2) = 1.34$ eV and an intramolecular O–O bond length $d(\text{O} - \text{O}) = 1.54$ Å, corresponding to a peroxo-like state.^{27–29} Indeed, as aforementioned, in this adsorption state we find excess population of the nonbonding $2\pi^*$ orbital of the adsorbed molecule; in this state the oxygen molecule is not paramagnetic any longer. The activated molecule dissociates readily with a dissociation barrier $\Delta E_{\text{T}}^{\text{diss}} < 0.1$ eV, and the dissociation results in lowering of the energy by 1.09 eV; in the dissociated state $d(\text{O} - \text{O}) = 3.88$ Å (see Figure 5(a)). Another bridge

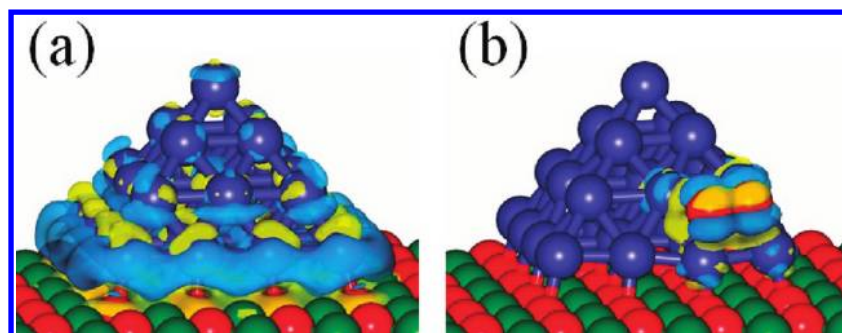


Figure 3. Isosurfaces of charge density differences $\Delta\rho(r)$ (drawn for a value corresponding to one that contains 70% of the charge) for: (a) the bare adsorbed cluster $\text{Pd}_{30}/\text{MgO}$, with $\Delta\rho(r) = \rho[\text{Pd}_{30}/\text{MgO}](r) - \rho[\text{Pd}_{30}](r) - \rho[\text{MgO}](r)$ and (b) for the adsorbed cluster and an oxygen molecule adsorbed close to the cluster/MgO surface interface, $\text{Pd}_{30}\text{O}_2/\text{MgO}$, with $\Delta\rho(r) = \rho[\text{Pd}_{30}\text{O}_2/\text{MgO}](r) - \rho[\text{Pd}_{30}\text{MgO}](r) - \rho[\text{O}_2](r)$. In (a) $\Delta Q[\text{Pd}_{30}/\text{MgO}] = 1.23e$, and in (b) $\Delta Q[\text{Pd}_{30}\text{O}_2/\text{MgO}] = 1.28e$. The charge difference on the adsorbed O_2 molecule is $\Delta Q[\text{O}_2] = 0.24e$, and on the four Pd atoms neighboring the adsorbed molecule $\Delta Q[4\text{Pd's near O}_2] = -0.1e$, indicating a transfer of charge from these atoms to the adsorbed molecule resulting in increased occupancy of the antibonding $2\pi^*$ and intrabond activation. For the bare cluster, the charge differences (per atom) are as follows: $\Delta Q[\text{L1}] = 0.045e$, $\Delta Q[\text{L2}] = 0.040e$, $\Delta Q[\text{L3}] = 0.03e$, $\Delta Q[\text{L4}] = 0.035e$. This shows that the largest charge difference (excess charge) is located in the first layer (L1) which contacts the MgO surface. Also, for that layer, the excess charge per surface (s) atom $\Delta Q[\text{L1;s}] = 0.053e$, while for an internal (i) atom $\Delta Q[\text{L1;i}] = 0.022e$. For $L = 3$ these values are: $\Delta Q[\text{L2;s}] = 0.045e$ and $\Delta Q[\text{L2;i}] = 0.013e$. The color scheme is as described in Figure 2. Excess charge isosurfaces are depicted in light blue, and charge depletion is given by yellow isosurfaces. Note the excess charge on the adsorbed molecule (bottom right corner in (b)), enveloped by charge depletion on the surrounding Pd atoms.

adsorption site at the second layer of the Pd cluster is shown in Figure 4(b), with a smaller adsorption energy, $\text{BE}(\text{O}_2) = 0.81$ eV, and an intramolecular O–O bond length, $d(\text{O}–\text{O}) = 1.47$ Å, also corresponding to a peroxo-like state. As in the previous

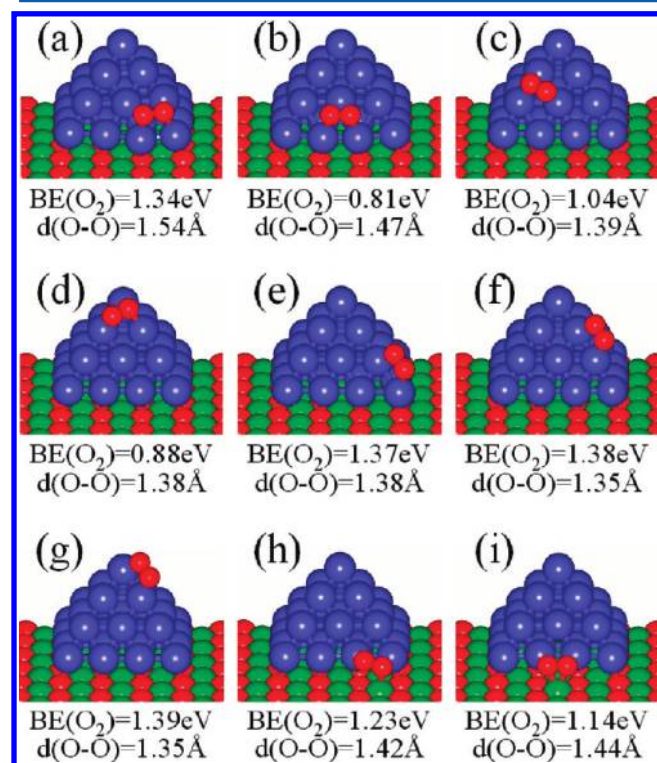


Figure 4. O_2 adsorptions on $\text{Pd}_{30}(\text{pyramidal})/\text{MgO}$. The binding (adsorption) energies of the O_2 molecules to the Pd cluster $\text{BE}(\text{O}_2)$ and the intramolecular distance $d(\text{O}–\text{O})$ are given below each of the adsorption configurations. Red balls represent adsorbed O_2 molecules. Pd atoms in blue. Mg atoms are described by the green balls and oxygen atoms of the MgO surface by red atoms in the $\text{MgO}(001)$ plane. The dissociation energies of some of the displayed configurations are: $\Delta E_{\text{T}}^{\text{diss}} < 0.1$ eV for (a) and (b), 0.61 eV for (c), 0.72 eV for (d), 1.51 eV for (f), and 1.34 eV for (g).

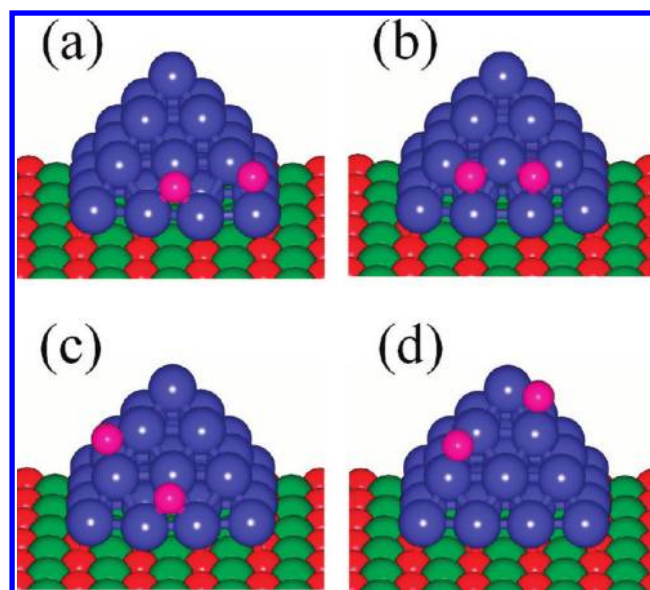


Figure 5. Dissociated states corresponding to the oxygen adsorption configurations (a–d) in Figure 4. Dissociation energies ($\Delta E_{\text{T}}^{\text{diss}}$): negligible for (a) and (b), $\Delta E_{\text{T}}^{\text{diss}} = 0.61$ eV for (c), and $\Delta E_{\text{T}}^{\text{diss}} = 0.72$ eV for (d). Distances between two oxygen atoms are: (a) 3.88 Å, (b) 3.13 Å, (c) 4.51 Å, and (d) 4.75 Å, respectively. Color designation is as in Figure 3, with the dissociated oxygen atoms depicted by pink balls.

case, dissociation of this adsorbed molecule is essentially barrierless, with $d(\text{O}–\text{O}) = 3.13$ Å after dissociation (Figure 5(b)).

The highest binding (adsorption) energies of the O_2 molecule were found for the edge sites (Figure 4(e,f,g)) with $\text{BE}(\text{O}_2) = 1.37$, 1.38, and 1.39 eV, respectively. However, the corresponding O–O bond lengths, $d(\text{O}–\text{O}) = 1.38$, 1.35, and 1.35 Å, for states e, f, and g, respectively, indicate a smaller degree of activation (superoxo-like state). The smaller activation of the adsorbed oxygen molecules is reflected by the rather high dissociation barrier energies associated with these states, e.g., $\Delta E_{\text{T}}^{\text{diss}} = 1.51$ and 1.34 eV for states (f) and (g), respectively. Additionally, we found that while the

interfacial O_2 binding states shown in Figure 4 (h,i) are characterized by relatively strong adsorption and peroxy-like O–O distances ($d(O-O) = 1.42 \text{ \AA}$, 1.44 \AA) their dissociation entails rather high (over 0.8 eV) dissociation barrier energies. In light of these observations, we conclude that the early stages of oxidation of the adsorbed Pd_{30}/MgO cluster will involve oxygen molecules adsorbed at bridge sites at the second layer of the supported Pd cluster (that is, Figure 4(a,b)), with subsequent dissociation involving oxygen molecules adsorbed at higher layers of the cluster, such as those shown in Figure 4(c,d).

To illustrate the oxidation mechanism of the adsorbed Pd cluster, we display in Figure 6 structures that correspond to oxidation steps, leading to the formation of the partially oxidized $Pd_{30}O_{10}/MgO$ cluster. We start in Figure 6(a) with a top view of the supported cluster with a singly adsorbed O_2 molecule, $Pd_{30}(O_2)/MgO$ (compare Figure 4(a), $BE(O_2) = 1.34 \text{ eV}$ and $d(O-O) = 1.54 \text{ \AA}$); here we denote in parentheses molecularly adsorbed oxygen molecules. The highly activated peroxy-like molecule dissociates readily, and a second molecule adsorbs on the opposite edge in a highly activated peroxy state; the resulting configuration corresponds to $Pd_{30}O_2(O_2)/MgO$. Dissociation of the adsorbed molecule and further adsorption of an additional molecule lead to formation of $Pd_{30}O_4(O_2)/MgO$ (Figure 6(c)) and following a similar step to $Pd_{30}O_6(O_2)$ (Figure 6(d)) which dissociates with essentially no activation barrier to form $Pd_{30}O_8$ (Figure 6(e)). Diffusional rearrangement (with negligible diffusion barriers) of the oxygen atoms along the edges of the cluster leads to the lower energy (0.8 eV) structure shown in Figure 6(f). Adsorption of a fifth O_2 molecule near the apex of the pyramidal cluster leads to $Pd_{30}O_8(O_2)$ (Figure 6(g)) which upon dissociation (entailing an energy barrier of 0.72 eV) results in $Pd_{30}O_{10}$ (Figure 6(h)). Structural relaxation, involving diffusion energy barriers of 0.2 eV , results in the final optimal partially oxidized cluster shown in Figure 6(i), with an energy gain of 1.85 eV .

Similar mechanisms, involving molecular adsorption, dissociation, and diffusional rearrangements, can be constructed for other partial oxidation states of the supported Pd_{30} cluster. We note however that the energy barriers involved in the formation of the $Pd_{30}O_{10}/MgO$ cluster described above were calculated to be smaller than those encountered in the formation of higher partial oxidation states. While in this paper we focus on the smallest partial oxidation state which allows interpretation of the main features of the CO oxidation reaction observed in the experiments (see Figure 1), it is likely that an ensemble of $Pd_{30}O_m/MgO$ clusters are formed (with their relative abundance governed by the partial oxidation kinetics and the ambient conditions).

In Figure 7, we show possible members of the $Pd_{30}O_m/MgO$ partial oxidation state ensemble, with $m = 10, 12, 14, 16$, and 24 . We note that in the fully oxidized cluster $Pd_{30}O_{24}/MgO$ (Figure 7(e)) the average energy per O atom is 0.6 eV lower than in the $Pd_{30}O_{10}/MgO$ cluster, reflecting the finding that the binding energy of O atoms at the lower layers of the oxidized Pd cluster is higher than in upper layers.

3.2.3. CO Oxidation Reaction. **3.2.3A. Multiple CO Coadsorption.** CO adsorption on the partially oxidized $Pd_{30}O_{10}/MgO$ cluster occurs preferentially on top of the Pd atom at the apex of the square pyramid. The binding energies of the CO molecule exhibit a dependence on the adsorption site, and they increase as a function of the distance of the site from the interface of the Pd cluster with the MgO surface; see

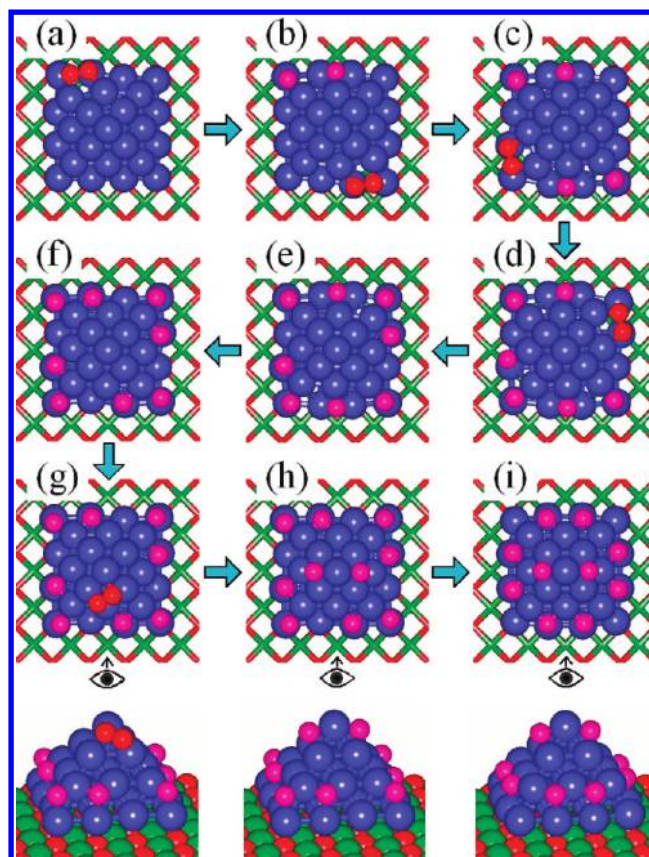


Figure 6. Oxidation of Pd_{30}/MgO resulting in formation of the partially oxidized cluster $Pd_{30}O_{10}/MgO$. For visual clarity, we denote by red balls newly adsorbed (undissociated) molecular O_2 , and pink balls denote dissociated oxygen atoms. In (a–i) we display top-down views of the system, with the center (blue) atom corresponding to the Pd atom at the apex of the square pyramid. The top layer of the MgO surface is described by sticks connecting the surface atoms; green sticks correspond to Mg and red ones to O atoms. At the bottom row, we show side views corresponding to the structures displayed in (g–i). The eye symbol indicates the direction from which the structures (h–i) are viewed. (a) Adsorption of the first O_2 molecule: $BE(O_2) = 1.34 \text{ eV}$ and $d(O-O) = 1.54 \text{ \AA}$. (b) Dissociation of the first O_2 molecule (transition state barrier $\Delta E_T < 0.1 \text{ eV}$) and adsorption of the second O_2 : $BE(O_2) = 1.31 \text{ eV}$ and $d(O-O) = 1.56 \text{ \AA}$. (c) Dissociation of the second O_2 ($\Delta E_T < 0.1 \text{ eV}$) and adsorption of the third O_2 molecule: $BE(O_2) = 1.45 \text{ eV}$ and $d(O-O) = 1.54 \text{ \AA}$. (d) Dissociation of the third O_2 molecule ($\Delta E_T < 0.1 \text{ eV}$) and adsorption of the fourth O_2 : $BE(O_2) = 1.38 \text{ eV}$ and $d(O-O) = 1.59 \text{ \AA}$. (e) Dissociation of the fourth O_2 molecule ($\Delta E_T < 0.1 \text{ eV}$). (f) Structure resulting from the diffusion of the oxygen atoms located initially at the center of the upper and lower edges in the figure (diffusion energy barriers are smaller than 0.1 eV). The energy of the structure in (f) is lower than that of the initial configuration (e) by 0.8 eV . (g) Adsorption of the fifth O_2 molecule: $BE(O_2) = 0.95 \text{ eV}$ and $d(O-O) = 1.38 \text{ \AA}$. (h) Dissociation of the fifth O_2 : $\Delta E_T = 0.72 \text{ eV}$. (i) Structure resulting from diffusion of the four corner oxygen atoms (diffusion energy barriers are 0.2 eV). The energy of this structure is lower by 1.85 eV compared to the energy of the initial state shown in (h).

Figure 8 where the optimized configuration of $Pd_{30}O_{10}(CO)_{13}/MgO$ is shown. The increased bond length of the adsorbed CO molecules indicates an activated state. The CO desorption (binding) energies indicated in Figure 8 correspond to the multiple CO adsorption configurations, and each was calculated as total energy difference $E_{des}[CO] = E[Pd_{30}O_{10}(CO)_{12}/MgO] + E[CO] - E[Pd_{30}O_{10}(CO)_{13}/MgO]$, where in each case of

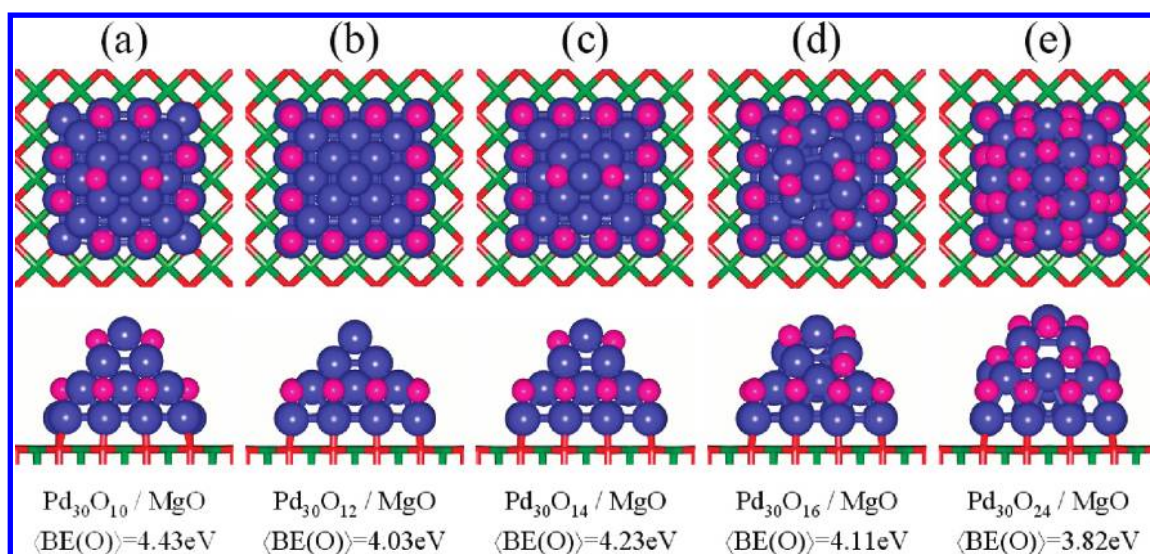


Figure 7. (a–e) Partially oxidized Pd_{30} ($\text{Pd}_{30}\text{O}_{10}$, $\text{Pd}_{30}\text{O}_{12}$, $\text{Pd}_{30}\text{O}_{14}$, and $\text{Pd}_{30}\text{O}_{16}$) and the fully oxidized $\text{Pd}_{30}\text{O}_{24}$ supported on a $\text{MgO}(001)$ surface. The average binding energy $\langle \text{BE}(\text{O}) \rangle$ is calculated by using the expression $[E(\text{Pd}_{30}) + mE(\text{O}) - E(\text{Pd}_{30}\text{O}_m)]/m$. (a) Average binding energy per atom of two oxygen atoms on top is 4.14 eV with respect to $\text{Pd}_{30}\text{O}_8/\text{MgO}$ (average binding energy per atom of the eight bottom oxygen atoms is 4.50 eV). (b) Average binding energy per atom of a bottom corner atom in (b) is 3.08 eV (with respect to the 8 noncorner atoms). (c) Average binding energy per atom of two oxygen atoms on top is 5.43 eV, with reference to the bottom 12 oxygen atoms. (d) Average binding energy per two oxygen atoms (located between the 2nd and 3rd layers of the Pd cluster) is 3.34 eV.

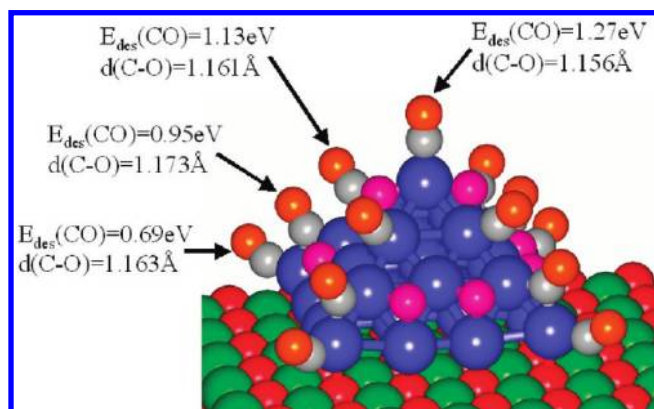


Figure 8. Multiple CO adsorption on the $\text{Pd}_{30}\text{O}_{10}/\text{MgO}$ cluster. Shown is an optimal configuration of $\text{Pd}_{30}\text{O}_{10}(\text{CO})_{13}/\text{MgO}$, with the desorption energies corresponding to removal of the corresponding CO molecule. Note the strong dependence of $E_{\text{des}}(\text{CO})$ on the adsorption site and the increasing trend of the desorption energy as a function of increasing distance from the interface of the Pd cluster with the MgO surface. The color designation is as indicated in Figure 6. Carbon atoms are represented by gray balls, and the oxygen atoms of the CO molecules are colored orange.

the 12 CO molecules (first term in the energy difference expression) a different CO molecule has been removed (see the four cases indicated by arrows in Figure 8).

3.2.3B. CO Oxidation Reaction. In this section, we discuss the atomic-scale reaction mechanisms underlying the catalyzed CO oxidation TPR profiles observed experimentally (Figure 1). As aforementioned, it is likely that an ensemble of partially oxidized Pd_{30} clusters corresponding to various degrees of oxidation coexist in thermodynamic equilibrium on the magnesia surface; this ensemble is likely to be formed during the higher-temperature oxygen pretreatment of the $\text{Pd}_{30}/\text{MgO}$ system prior to cooling to cryogenic conditions (120 K) and exposure to CO, as well as to isotopic $^{18}\text{O}_2$. Our strategy is to explore the reaction pathways involving a minimal partially

oxidized supported Pd_{30} cluster that would allow a consistent description of the main observed features of the CO oxidation reaction and its temperature dependence. To this aim, we investigate various reaction mechanisms involving the partially oxidized $\text{Pd}_{30}\text{O}_{10}/\text{MgO}$ cluster. In this context, it is pertinent to note that for the particular conditions of the experiments whose results we display in Figure 1 (i.e., pretreatment of the Pd_{30} clusters with O_2 at 370 K followed by annealing at 450 K) higher oxidation levels of the magnesia-supported Pd_{30} cluster are unfavorable.

Several atomic configurations of the model catalyst system corresponding to selected CO oxidation reaction processes on the partially oxidized $\text{Pd}_{30}\text{O}_{10}(\text{CO})_{13}/\text{MgO}$ model catalyst are displayed in Figure 9, with cyan and white arrows pointing to the CO molecule and oxygen atom that directly participate in the reaction. The reactions described in Figure 9 are characterized by transition state (TS) activation barriers in the range of $0.4 \text{ eV} \leq \Delta E_{\text{T}} \leq 0.7 \text{ eV}$, corresponding to the lower-temperature peaks (α and β) in the TPR experiments (Figure 1). Subsequently, we show in Figure 10 the atomic configuration developing after completion of the lower-activation energy reactions at the early part (lower temperatures) of the temperature-programmed ramp. The configurations in Figure 10 correspond to higher-temperature scenarios (peaks γ and δ in the TPR experiments, see Figure 1) with $\Delta E_{\text{T}} \geq 0.8\text{--}0.9 \text{ eV}$.

The lowest reaction temperature for which oxidation of CO was detected in the experiments was $\sim 180 \text{ K}$ (see Figure 1 where the α peak corresponds to the formation of the $\text{C}^{16}\text{O}^{18}\text{O}$ isotopomer, resulting from a LH-type reaction between an adsorbed C^{16}O and a molecularly (interfacially) adsorbed $^{18}\text{O}_2$, and see the atomic configuration of $\text{Pd}_{30}\text{O}_{10}(\text{O}_2)(\text{CO})_{13}/\text{MgO}$ in Figure 9(a)). Indeed, this reaction has been found to be characterized by a pathway (see Figure 11) exhibiting a low transition state (TS) activation energy barrier $\Delta E_{\text{T}} = 0.40 \text{ eV}$, corresponding to the above low-temperature reaction (i.e., α) mechanism. Only a limited number of configurations were

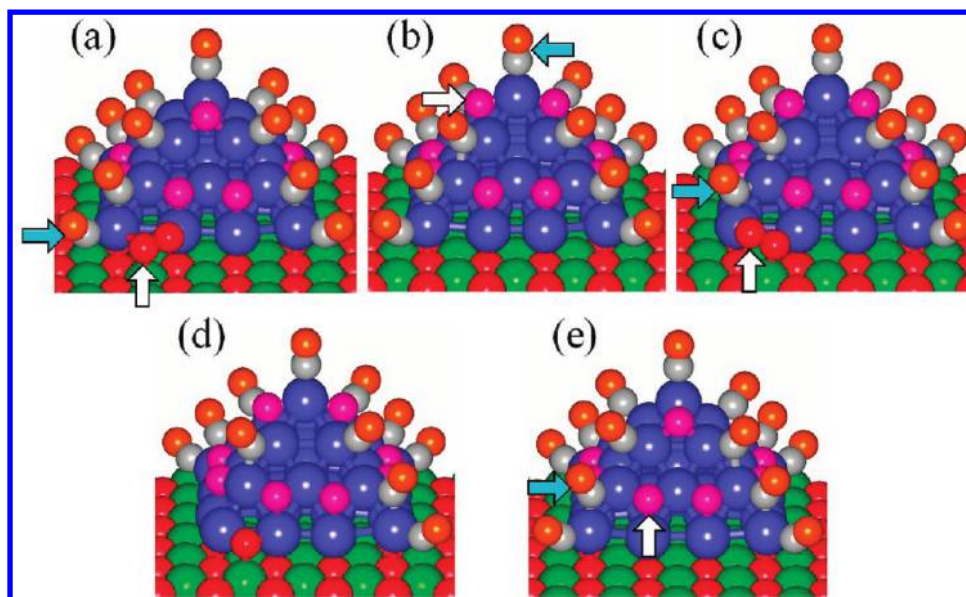


Figure 9. Atomic configurations of the partially oxidized Pd_{30} cluster supported on $\text{MgO}(100)$ with multiple coadsorbed CO molecules, corresponding to selected CO oxidation reaction processes. Cyan and white arrows point to the CO molecule and oxygen atom that directly participate in the reaction. (a) $\text{Pd}_{30}\text{O}_{10}(\text{O}_2)(\text{CO})_{13}/\text{MgO}$ with the binding energies and bond lengths of the reactant molecules given by: $\text{BE}(\text{O}_2) = 0.50$ eV, $d(\text{O}-\text{O}) = 1.36$ Å, and $\text{BE}(\text{CO}) = 0.69$ eV, $d(\text{C}-\text{O}) = 1.162$ Å. The TS activation energy of the LH reaction is $\Delta E_{\text{T}} = 0.40$ eV corresponding to the $^{13}\text{C}^{16}\text{O}^{18}\text{O}$ α signals in the experimental data shown in Figure 1. (b) $\text{Pd}_{30}\text{O}_{10}(\text{CO})_{13}/\text{MgO}$ with $\text{BE}(\text{CO}) = 1.27$ eV and $d(\text{C}-\text{O}) = 1.156$ Å (see Figure 8). The transition state (TS) activation energy of the MvK oxidation reaction is $\Delta E_{\text{T}} = 0.50$ eV, corresponding to the onset of the $^{13}\text{C}^{16}\text{O}^{16}\text{O}$ β signal in the experimental data (Figure 1). (c) $\text{Pd}_{30}\text{O}_{10}(\text{O}_2)(\text{CO})_{13}/\text{MgO}$, with the binding energies and bond length of the reacting molecules given by: $\text{BE}(\text{O}_2) = 0.84$ eV, $d(\text{O}-\text{O}) = 1.40$ Å, and $\text{BE}(\text{CO}) = 1.36$ eV, $d(\text{C}-\text{O}) = 1.169$ Å. The TS activation energy of the LH reaction is $\Delta E_{\text{T}} = 0.66$ eV corresponding to the $^{13}\text{C}^{16}\text{O}^{18}\text{O}$ β signal in Figure 1. (d) The $\text{Pd}_{30}\text{O}_{11}(\text{CO})_{12}/\text{MgO}$ system resulting from the reaction in (c), after CO_2 ejection. (e) $\text{Pd}_{30}\text{O}_{10}(\text{CO})_{13}/\text{MgO}$ with $\text{BE}(\text{CO}) = 1.13$ eV, $d(\text{C}-\text{O}) = 1.173$ Å. The TS activation energy of the MvK reaction is $\Delta E_{\text{T}} = 0.60$ eV, corresponding to the $^{13}\text{C}^{16}\text{O}^{16}\text{O}$ β signals in the experimental data shown in Figure 1.

found by us to give activation barriers in this low-energy range, correlating with the low amplitude of the experimentally measured α -peak in Figure 1. On the other hand, we found several atomic configurations corresponding to reactions with activation barriers in the 0.5–0.8 eV range, reflecting the higher amplitude of the β -peak occurring at higher temperature (see Figure 1); note that the feature marked β has been measured for both the $\text{C}^{16}\text{O}^{16}\text{O}$ and $\text{C}^{16}\text{O}^{18}\text{O}$ isotopomers. Examples of atomic configurations leading to such reactions are given in the following: (i) An MvK reaction shown in Figure 9(b) for $\text{Pd}_{30}\text{O}_{10}(\text{CO})_{13}/\text{MgO}$ with $\Delta E_{\text{T}} = 0.50$ eV, corresponding to the onset of the $\text{C}^{16}\text{O}^{16}\text{O}$ β -peak in Figure 1. We note here that the binding energy of the $^{18}\text{O}_2$ molecule in Figure 9(a) was found to be sufficiently low (0.5 eV) to allow thermal desorption of the molecularly adsorbed oxygen molecule (see the O_2 molecule marked by a white arrow, at the cluster–magnesia interface in Figure 9(a)), leading to generation of the configuration shown in Figure 9(b). (ii) An LH reaction shown in Figure 9(c), where we display a $\text{Pd}_{30}\text{O}_{10}(\text{O}_2)(\text{CO})_{13}/\text{MgO}$ configuration (with a sufficiently high binding energy of the interfacially bound molecular oxygen, i.e., $\text{BE}(\text{O}_2) = 0.84$ eV, to resist desorption upon heating), that participates in a CO oxidation reaction with $\Delta E_{\text{T}} = 0.66$ eV. This reaction contributes to the $\text{C}^{16}\text{O}^{18}\text{O}$ β -peak in Figure 1. The product $\text{Pd}_{30}\text{O}_{11}(\text{CO})_{12}/\text{MgO}$ cluster configuration of the above reaction is shown in Figure 9(d) (see also Figure 10(a)). (iii) Another MvK reaction shown in Figure 9(e), displaying a configuration of $\text{Pd}_{30}\text{O}_{10}(\text{CO})_{13}/\text{MgO}$ that participates in a CO oxidation reaction with $\Delta E_{\text{T}} = 0.60$ eV, whose pathway is shown in Figure 12, contributing to the $\text{C}^{16}\text{O}^{16}\text{O}$ β -peak in Figure 1.

The reactions occurring at the earlier stages of the temperature ramp in the TPR experiments corresponding to transition state activation energies, ΔE_{T} , of up to 0.8 eV deplete the reactants adsorbed on the Pd cluster. Consequently, in our discussion of CO oxidation reactions catalyzed at higher temperatures, we focus on scenarios which involve only a few reacting species. We start with the two adsorbed oxygen configurations shown in Figure 10(a). This configuration may evolve from the one shown in Figure 9(d) that results from the LH reaction described in Figure 9(c) and subsequent lower-temperature reactions of the remaining adsorbents. We note that one of the atoms (the one colored red, near the left corner at the bottom interface between the Pd cluster and the magnesia surface) originated from an $^{18}\text{O}_2$ isotopomer, while the oxygen atom on the right (colored purple), adsorbed on the second layer of the Pd cluster, is an ^{16}O atom that originated from the high-temperature oxygen pretreatment of the cluster. Upward hopping diffusion of the ^{18}O atom (involving an activation barrier of 0.8 eV) results in the configuration shown in Figure 10(b), which may undergo an MvK reaction with a CO molecule; CO molecules were found to diffuse readily on the Pd cluster, with typical diffusion barriers being of the order of 0.5–0.6 eV. Furthermore, CO molecules may reach the adsorbed cluster from the support surface via reverse spillout. The configuration in Figure 10(c) leads to an MvK CO oxidation reaction with an activation barrier $\Delta E_{\text{T}} = 0.86$ eV, and since it may involve either of the adsorbed oxygen atoms it may contribute to the higher-temperature γ -peaks (for both the $\text{C}^{16}\text{O}^{16}\text{O}$ and $\text{C}^{16}\text{O}^{18}\text{O}$ isotopomer) observed in the TPR data shown in Figure 1. Other high activation energy oxidation reactions contributing to the γ -peak are shown in Figures

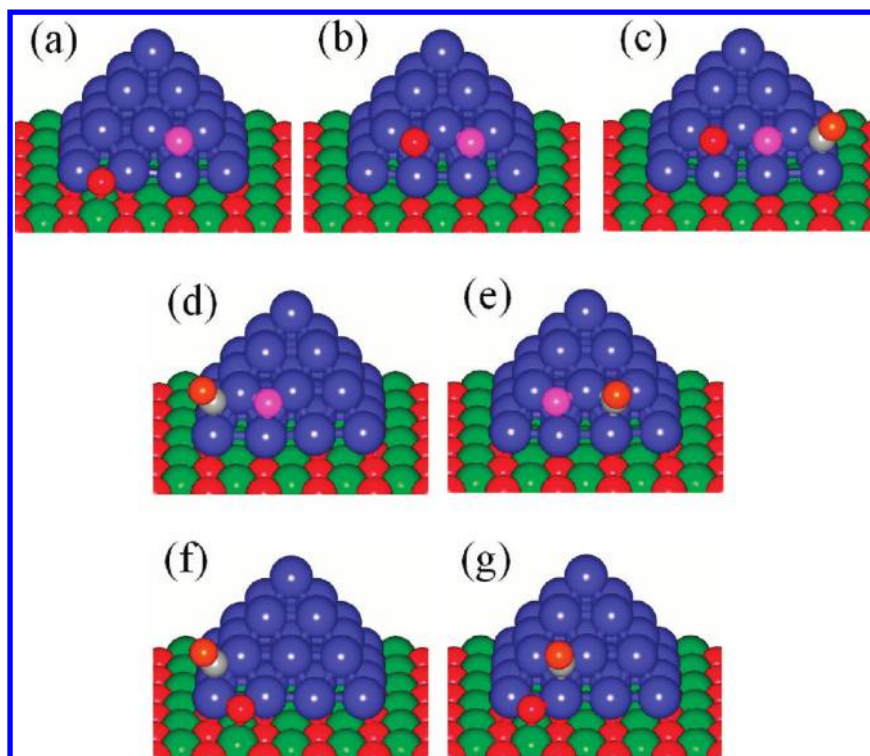


Figure 10. Atomic configuration involved in higher-temperature CO oxidation processes. (a) Two oxygen atoms adsorbed on Pd₃₀/MgO. The oxygen atom (red ball) on the bottom Pd layer is the ¹⁸O atom remaining from the LH reaction ¹³C¹⁶O + ¹⁸O₂ (see the LH reaction in Figure 9(c) resulting in the configuration shown in Figure 9(d)), and the other one (pink ball) is an ¹⁶O atom from the initial partially oxidized Pd₃₀¹⁶O₁₀/MgO. Average binding energy per atom for the two oxygen atoms (red + pink) is $\langle \text{BE}(\text{O}) \rangle = 4.24$ eV. Desorption energy of the bottom oxygen atom (red) is 4.04 eV, and that of the upper atom (pink) is 4.48 eV. (b) The atomic configuration achieved subsequent to upward diffusion of the ¹⁸O atom (red) from the bottom layer of the Pd cluster (see (a)). The diffusion process entailed two hopping events (each to the nearest 3-fold hollow site on the Pd cluster facet) with activation energies of 0.8 and 0.2 eV. Average binding energy per atom is $\langle \text{BE}(\text{O}) \rangle = 4.32$ eV. Desorption energy of an oxygen atom (either red or pink) is 4.21 eV. (c) CO oxidation reaction involving either of the oxygen atoms shown in (b). The TS activation energy of the MvK reaction is $\Delta E_{\text{T}} = 0.86$ eV, and it corresponds to the γ signals of ¹³C¹⁶O¹⁶O or ¹³C¹⁶O¹⁸O in the experimental data shown in Figure 1 (depending on whether the CO is adsorbed on the right or left corner-bridge site; in either case $\text{BE}(\text{CO}) = 1.99$ eV and $d(\text{C}-\text{O}) = 1.182$ Å). (d) Atomic configuration of the reaction of CO ($\text{BE}(\text{CO}) = 2.03$ eV) with a single ¹⁶O adsorbed atom with $\text{BE}(\text{O}) = 4.44$ eV. The TS activation energy of the MvK reaction yielding ¹³C¹⁶O¹⁶O is $\Delta E_{\text{T}} = 1.00$ eV corresponding to the γ peaks in the experiments shown in Figure 1. (e) Atomic configuration of the reaction of CO ($\text{BE}(\text{CO}) = 2.01$ eV) with a single ¹⁶O adsorbed atom with $\text{BE}(\text{O}) = 4.44$ eV. The TS activation energy of the MvK reaction yielding ¹³C¹⁶O¹⁶O is $\Delta E_{\text{T}} = 1.16$ eV corresponding to the δ peaks in the experiments shown in Figure 1. (f) Atomic configuration of the reaction of CO ($\text{BE}(\text{CO}) = 2.01$ eV) with a single ¹⁸O adsorbed atom with $\text{BE}(\text{O}) = 4.00$ eV. The TS activation energy of the MvK reaction yielding ¹³C¹⁶O¹⁸O is $\Delta E_{\text{T}} = 0.89$ eV corresponding to the γ peaks in the experiments shown in Figure 1 (lower curve). (g) Atomic configuration of the reaction of CO ($\text{BE}(\text{CO}) = 2.14$ eV) with a single ¹⁸O adsorbed atom with $\text{BE}(\text{O}) = 4.00$ eV. The TS activation energy of the MvK reaction yielding ¹³C¹⁶O¹⁸O is $\Delta E_{\text{T}} = 1.16$ eV corresponding to the δ peak in the experiments shown in Figure 1 (lower curve).

10(d), with $\Delta E_{\text{T}} = 1.00$ eV, and Figure 10(f), with $\Delta E_{\text{T}} = 0.89$ eV. Finally, we illustrate in Figures 10(e) ($\Delta E_{\text{T}} = 1.16$ eV) and 10(f) ($\Delta E_{\text{T}} = 1.15$ eV) configurations that may contribute (for both the ¹³C¹⁶O¹⁶O and ¹³C¹⁶O¹⁸O isotopomers) to the highest reaction temperature peak observed in the TPR experiments (marked δ in Figure 1). We remark that in the experiments the δ reaction mechanism is observed mainly for the ¹⁶O isotopomer. We attribute this finding to the much higher population of this isotopomer (employed in the cluster pretreatment stage) in comparison with the ¹⁸O isotopomer used in the cryogenic dosing stage; the latter isotopomer is likely to be consumed by the lower-temperature (β and γ) mechanisms in the TPR experiments, thus greatly depleting its population at the higher temperatures.

4. SUMMARY

In this paper, we report on experimental and theoretical investigations of the oxidation reaction of CO to form carbon dioxide, catalyzed by size-selected Pd₃₀ clusters soft-landed on

MgO(100). In the experiments, we investigate the consequences of pretreatment of the deposited clusters with molecular oxygen at a temperature of ~ 370 K in an ¹⁶O₂ background followed by annealing at around 450 K. Subsequent to the above pretreatment stage, the system was cooled to 120 K, and after exposure to ¹⁸O₂ and ¹³C¹⁶O the temperature was ramped and a TPR spectrum recorded. The onset of the catalyzed CO combustion was found to occur at a low temperature of 180 K, and the TPR spectrum showed oxidation of CO over a broad temperature range extending to 550 K (see Figure 1(a)).

Using first-principles density functional theory calculations, we investigated first the adsorption geometry of the Pd₃₀ cluster on the MgO(100) surface. A square-base pyramidal structure was found to be energy optimal (Figure 2), with an excess electronic charge of $\sim 1.25e$ (originating from the underlying magnesia support) found to be localized near the interfacial region of the cluster with the supporting surface (Figure 3(a)). The degree of charge transfer from the surface is rather insensitive to the adsorption of an oxygen molecule; compare

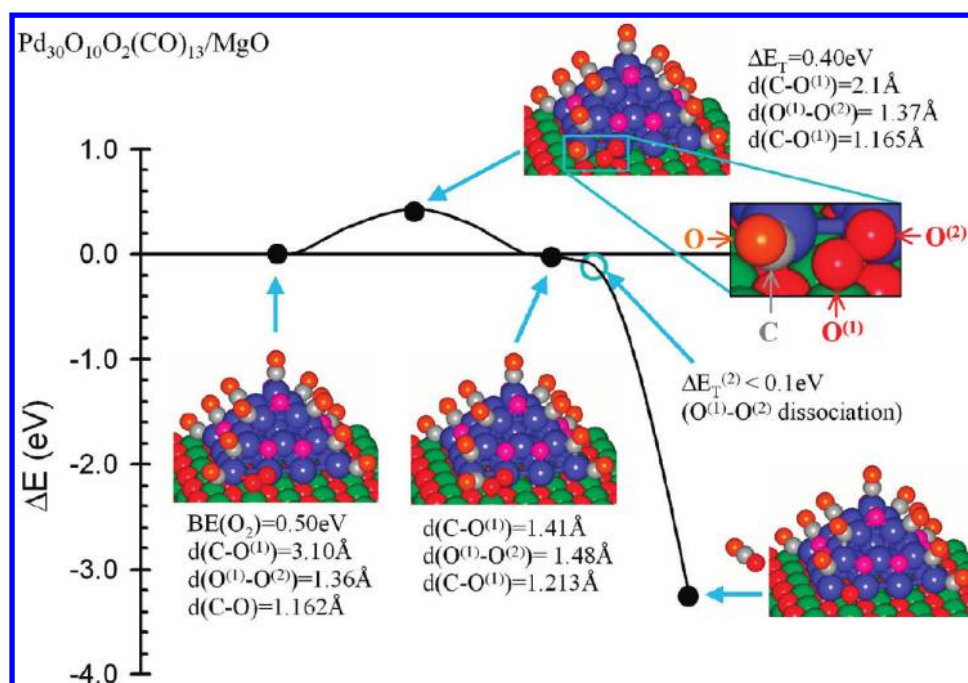


Figure 11. Reaction path for the CO oxidation reaction corresponding to the Langmuir–Hinshelwood (LH) low-temperature α peak ($\text{C}^{16}\text{O}^{18}\text{O}$) in the experimental data (Figure 1, lower curve). The reaction starts from $\text{Pd}_{30}\text{O}_{10}(\text{O}_2)(\text{CO})_{13}/\text{MgO}$ (taken as the reference energy scale), with the $^{18}\text{O}_2$ molecule (depicted by red balls) adsorbed (with $\text{BE}(\text{O}_2) = 0.50$ eV) at the interface of the cluster with the magnesia surface, forming $\text{Pd}_{30}\text{O}_{10}(\text{O}_2)(\text{CO})_{13}/\text{MgO}$ (see also Figure 9(a)). Surmounting a rather low transition state activation barrier ($\Delta E_T = 0.40$ eV, see zoomed-in TS configuration), the reaction results in the ejection of $\text{C}^{16}\text{O}^{18}\text{O}$ in a highly exothermic process. Color designation as in the previous figures.

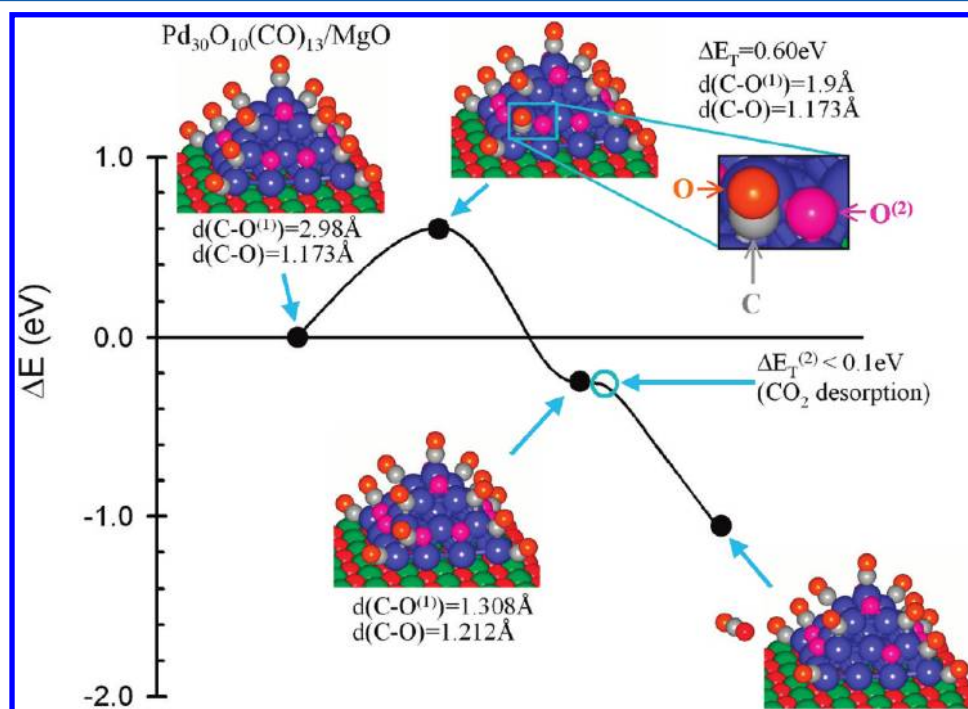


Figure 12. Reaction path for the CO oxidation reaction corresponding to the MvK reaction corresponding to the $\text{C}^{16}\text{O}^{16}\text{O}$ β peak observed experimentally in the temperature range of 300–360 K (see Figure 1). The reaction starts from $\text{Pd}_{30}\text{O}_{10}(\text{CO})_{13}/\text{MgO}$ (taken as the reference energy scale), where the distance between the C atom of the reacting CO molecule and the reacting oxygen atom $d(\text{CO}^{(1)}) = 2.98$ Å; see also Figure 9(e). The transition state configuration is reached when the distance between the reactants is reduced to 1.9 Å, entailing the climbing of a TS activation barrier of 0.6 eV. Subsequently, the reaction proceeds through the ejection of $\text{C}^{16}\text{O}^{16}\text{O}$ in a highly exothermic process. Color designation as in the previous figures.

the values in Figure 3(a) and 3(b). However, upon oxygen adsorption, charge (0.25e) is transferred to the O_2 molecule from the neighboring Pd atoms of the cluster. This excess

charge increases the occupancy of the antibonding $2\pi^*$ orbital of the adsorbed molecule (Figure 3(b)), with consequent activation to a peroxo state characterized by an increased

interoxygen bond length (see Figure 4(a)). Moreover, the adsorption of five oxygen molecules exhausts the excess charge (1.25e) on the Pd cluster, and consequently further adsorbed oxygen molecules are activated to a smaller degree resulting in higher dissociation energy barriers. This contributes to the self-limiting nature of the oxidation process of the supported Pd₃₀ nanocluster.

Subsequently, we explored rather exhaustively structural and energetic properties of a variety of oxygen adsorption sites on the supported palladium cluster and effects due to multiple adsorbed O₂ molecules (Figures 4–6). We show that the barriers for dissociation of the adsorbed molecules depend strongly on the location of the adsorption site on the supported pyramidal Pd₃₀ cluster (Figures 4 and 5). The transition state for dissociation is very small (<0.1 eV) for adsorption sites (on the cluster) that are closer to the cluster interface with the Mg(100) surface (Figure 5(a) and (b)), correlating with the aforementioned activation (that is, lower dissociation barriers) of molecules adsorbed at these sites due to increased occupancy of their antibonding 2π* orbitals. Further oxygen dissociation processes which occur beyond the close cluster-to-surface interfacial region, involving adsorption sites located at larger distances from the interface, entail much larger dissociation barriers, resulting in self-limiting partial oxidation of the Pd₃₀ cluster. Consequently, our theoretical analysis of the CO oxidation reaction focuses on a partially oxidized Pd₃₀O₁₀ cluster (Figure 7).

Using the information obtained through isotope labeling in the TPR experiments (where the two isotopomers, ¹³C¹⁶O¹⁶O and ¹³C¹⁶O¹⁸O, were detected mass spectrometrically during the temperature ramp), we explored through first-principles quantum simulations various reaction pathways, with a focus on the multiply coadsorbed system Pd₃₀O₁₀(CO)₁₃/MgO (see Figure 8). These theoretical calculations allowed us to correlate the measured isotope and temperature-dependent TPR features, with operative LH and MvK-type reaction mechanisms catalyzed by the partially oxidized cluster (Figures 9 and 10). The LH mechanism was found to contribute to the reaction at lower temperatures (see, e.g., Figure 11), while the MvK dominates for higher temperatures (see Figure 12).

To conclude, we remark that the work presented in this paper forms a solid foundation for future multitechnique research efforts on this nanocatalytic model system, employing experimental techniques which may include: ultraviolet and X-ray photoemission spectroscopy (UPS and XPS), medium-energy ion scattering (MEIS), and scanning tunneling and force microscopy (STM and AFM). With the use of these techniques, as well as pulsed molecular beam measurements and experiments using microreactors operating at ambient pressures, and in close coordination with large-scale first-principles theoretical investigations, we expect to gain further deep insights into the fundamental processes of supported metal cluster oxidation and catalytic reactivity.

AUTHOR INFORMATION

Corresponding Author

*E-mail: uzi.landman@physics.gatech.edu.

Notes

The authors declare no competing financial interest.

ACKNOWLEDGMENTS

The work of UL and BY at the Georgia Institute of Technology was supported by a grant from the US Air Force Office of Scientific Research (AFOSR). The work of UH at the Technical University of Munich and MM at the University of Freiburg was supported by the Deutsche Forschungsgemeinschaft within the priority program SPP1153 'Clusters on Surfaces'. UH acknowledges also support by the Deutsche Forschungsgemeinschaft within the project He3454/9-2. He also acknowledges the contribution of Florian Schweinberger at the beginning of this work. Calculations were performed at the Georgia Institute of Technology Center for Computational Materials Science.

REFERENCES

- (1) *Handbook of Heterogeneous Catalysis*; Ertl, G., Knoezinger, H., Weitkamp, J., Eds.; VCH: Weinheim, Germany, 1997.
- (2) Thomas, J. M.; Thomas, W. J. *Principles and Practice of Heterogeneous Catalysis*; VCH: Weinheim, Germany, 1997.
- (3) Engel, T.; Ertl, G. *J. Chem. Phys.* **1978**, *69*, 1267–1281.
- (4) See Supporting Information in: Kaden, E. W.; Kunkel, W. A.; Kane, M. D.; Roberts, S.; Anderson, S. L. *J. Am. Chem. Soc.* **2010**, *132*, 13097–13099.
- (5) Lamgmuir, I. *Trans. Faraday Soc.* **1922**, *17*, 1672.
- (6) Boudart, M.; Djega-Maxiadassou, G., *Kinetics of Heterogeneous Catalytic Reactions*; Princeton University Press: Princeton, N.J., 1984.
- (7) McClure, S. M.; Goodman, D. W. *Chem. Phys. Lett.* **2009**, *469*, 1–13.
- (8) Hinshelwood, C. N. *The Kinetics of Chemical Change in Gaseous Systems*; Clarendon Press: Oxford, 1933.
- (9) Doornkamp, C.; Ponc, V. J. *Mol. Catal. A: Chem.* **2000**, *162*, 19–32.
- (10) Pease, R. N.; Taylor, H. S. *J. Am. Chem. Soc.* **1922**, *44*, 1637–1647.
- (11) Kroger, C. Z. *Anorg. Chem.* **1932**, *206*, 289–303.
- (12) Mars, P.; van Krevelen, D. W. *Chem. Eng. Sci.* **1954**, *3*, 41–59.
- (13) Mars, P.; Maessen, J. G. H. In *Proceedings of the third ICC, Amsterdam, 1954*; North-Holland: Amsterdam, 1954; Vol. 1P, p 39.
- (14) Boreksov, G. K. In *Catalysis Science and Technology*; Anderson, J. R., Boudart, M., Eds.; Springer: Berlin, 1982; Vol. 3, p 39.
- (15) Croft, L. *Nat. Chem.* **2010**, *2*, 1009–1009.
- (16) Gandhi, H. S.; Graham, G. W.; McCabe, R. W. *J. Catal.* **2003**, *216*, 433–442.
- (17) Centi, G.; Ciambelli, P.; Perathoner, S.; Russo, P. *Catal. Today* **2002**, *75*, 3–15.
- (18) Cuenya, B. R. *Thin Solid Films* **2010**, *518*, 3127–3150.
- (19) Schalow, T.; Brandt, B.; Laurin, M.; Schauermaun, S.; Libuda, J.; Freund, H.-J. *J. Catal.* **2006**, *242*, 58–70.
- (20) Lundgren, E.; Kresse, G.; Klein, C.; Borg, M.; Andersen, J. N.; DeSantis, M.; Gauthier, Y.; Konvicka, C.; Schmid, M.; Varga, P. *Phys. Rev. Lett.* **2002**, *88*, 246103–1–246103–4.
- (21) Zemlyanov, D.; et al. *Surf. Sci.* **2006**, *600*, 983–994.
- (22) Gabasch, H.; Knop-Gericke, A.; Schlögl, R.; Borasio, M.; Weilach, Ch.; Rupprechter, G.; Penner, S.; Jenewein, B.; Hayek, K.; Klötzer, B. Comparison of the reactivity of different Pd-O species in CO oxidation. *Phys. Chem. Chem. Phys.* **2006**, *9*, 533–540.
- (23) (a) Conrad, H.; Ertl, G.; Küppers, J. *Surf. Sci.* **1978**, *76*, 323. (b) Engel, T.; Ertl, G. *Adv. Catal.* **1979**, *28*, 1–78.
- (24) Bernhardt, T. M.; Heiz, U.; Landman, U. In *Nanocatalysis*; Heiz, U., Landman, U., Eds.; Springer: Berlin, 2007; pp 1–191.
- (25) Landman, U.; Yoon, B.; Zhang, C.; Heiz, U.; Arenz, M. *Top. Catal.* **2007**, *44*, 145–158.
- (26) Sanchez, A.; Abbet, S.; Heiz, U.; Schneider, W. D.; Hakkinen, H.; Barnett, R. N.; Landman, U. *J. Phys. Chem. A* **1999**, *103*, 9573–9578.
- (27) Hakkinen, H.; Abbet, W.; Sanchez, A.; Heiz, U.; Landman, U. *Angew. Chem., Int. Ed.* **2003**, *42*, 1297–1300.

- (28) Yoon, B.; Hakkinen, H.; Landman, U.; Worz, A. S.; Antonietti, J. M. M.; Abbet, S.; Judai, K.; Heiz, U. *Science* **2005**, *307*, 403–407.
- (29) Harding, C.; Habibpour, V.; Kunz, S.; Farnbacher, A. N.-S.; Heiz, U.; Yoon, B.; Landman, U. *J. Am. Chem. Soc.* **2009**, *131*, 538–548.
- (30) Schalow, T.; Laurin, M.; Brandt, B.; Schauermaun, S.; Guimond, S.; Kuhlenbeck, H.; Starr, D. E.; Shaikhutdinov, S. K.; Libuda, J.; Freund, H.-J. *Angew. Chem., Int. Ed.* **2005**, *44*, 7601–7605.
- (31) Schalow, T.; Brandt, B.; Starr, D. E.; Laurin, M.; Shaikhutdinov, S. K.; Schauermaun, S.; Libuda, J.; Freund, H.-J. *Angew. Chem., Int. Ed.* **2006**, *45*, 3693–3697.
- (32) Nolte, P.; Stierle, A.; Kasper, N.; Jin-Phillipp, N. Y.; Reichert, H.; Rühm, A.; Okasinski, J.; Dosch, H. *Phys. Rev. B* **2008**, *77*, 115444–1–115444–7.
- (33) Schalow, T.; Brandt, B.; Laurin, M.; Guimond, S.; Starr, D. E.; Shaikhutdinov, S. K.; Schauermaun, S.; Libuda, J.; Freund, H.-J. *Top. Catal.* **2007**, *42–43*, 387–391.
- (34) Socaciu, L. D.; Hagen, J.; Bernhardt, T. M.; Woste, L.; Heiz, U.; Hakkinen, H.; Landman, U. *J. Am. Chem. Soc.* **2003**, *125*, 10437–10445.
- (35) Lang, S. M.; Bernhard, T. M.; Barnett, R. N.; Landman, U. *J. Am. Chem. Soc.* **2009**, *131*, 8939–8951.
- (36) Lang, S. M.; Bernhard, T. M.; Barnett, R. N.; Landman, U. *Angew. Chem., Int. Ed.* **2010**, *49*, 980–983.
- (37) Lang, S. M.; Bernhard, T. M.; Barnett, R. N.; Landman, U. *J. Phys. Chem. A* **2011**, *115*, 6788–6795.
- (38) (a) Harding, C. J.; Kunz, S.; Habibpour, V.; Heiz, U. *Phys. Chem. Phys.* **2008**, *10*, 5875–5881. (b) Kunz, S.; Schweinberger, F. F.; Habibpour, V.; Rottgen, M.; Harding, C.; Arenz, M.; Heiz, U. *J. Phys. Chem. C* **2010**, *114*, 1651–1654.
- (39) Kaden, W. E.; Wu, T.; Kunkel, W. A.; Anderson, S. L. *Science* **2009**, *326*, 826–829.
- (40) Moseler, M.; Hakkinen, H.; Landman, U. *Phys. Rev. Lett.* **2002**, *89*, 176103–1–176103–4.
- (41) Abbet, S.; Heiz, U.; Hakkinen, H.; Landman, U. *Phys. Rev. Lett.* **2001**, *86*, 5950–5953.
- (42) Huber, B.; Koskinen, P.; Häkkinen, H.; Moseler, M. *Nat. Mater.* **2006**, *5*, 44–47.
- (43) Walter, M.; Moseler, M. *Phys. Status Solidi B* **2010**, *247*, 1016–1022.
- (44) Abbet, S.; Judai, K.; Klinger, L.; Heiz, U. *Pure Appl. Chem.* **2002**, *74*, 1527–1535.
- (45) Heiz, U.; Vanolli, F.; Trento, T.; Schneider, W. D. *Rev. Sci. Instrum.* **1997**, *68*, 1986–1994.
- (46) Abbet, S.; Riedo, E.; Brune, H.; Heiz, U.; Ferrari, A. M.; Giordano, L.; Pacchioni, G. *J. Am. Chem. Soc.* **2001**, *123*, 6172–6178.
- (47) Di Valentin, C.; Del Vito, A.; Pacchioni, G.; Abbet, S.; Worz, A. S.; Judai, K.; Heiz, U. *J. Phys. Chem. B* **2002**, *106*, 11961–11969.
- (48) Kresse, G.; Hafner, J. *Phys. Rev. B* **1993**, *47*, R558–R561.
- (49) G. Kresse, G.; J. Furthmüller, J. *Phys. Rev. B* **1996**, *54*, 11169–11186.
- (50) Perdew, J. P.; Chevary, J. A.; Vosko, S. H.; Jackson, K. A.; Pederson, M. R.; Singh, D. J.; Fiolhais, C. *Phys. Rev. B* **1992**, *46*, 6671–6687.
- (51) Vanderbilt, D. *Phys. Rev. B* **1990**, *41*, 7892–7695.
- (52) Huber, K. P.; Herzberg, G. *Molecular Spectra and Molecular Structure IV. Constants of Diatomic Molecules*; Van Nostrand, Reinhold: New York, NY, 1979.
- (53) Moseler, M.; Walter, M.; Yoon, B.; Landman, U.; Habibpour, V.; Harding, C.; Kunz, S.; Heiz, H. Submitted.
- (54) Moseler, M.; Hakkinen, H.; Barnett, R. N.; Landman, U. *Phys. Rev. Lett.* **2001**, *86*, 2545–2548.